


Assessing Matched Filtering for Core-Collapse Supernova Gravitational-Wave Detection

Haakon Andresen¹ *, Bella Finkel²

¹*The Oskar Klein Centre, Department of Astronomy, Stockholm University, AlbaNova, SE-106 91 Stockholm, Sweden*

²*Department of Mathematics, University of Wisconsin–Madison, Madison, Wisconsin, 53703, USA*

Accepted XXX. Received YYY; in original form ZZZ

ABSTRACT

Gravitational waves from core-collapse supernovae are a promising yet challenging target for detection due to the stochastic and complex nature of these signals. Conventional detection methods for core-collapse supernovae rely on excess energy searches because matched filtering has been hindered by the lack of well-defined waveform templates. However, numerical simulations of core-collapse supernovae have improved our understanding of the gravitational wave signals they emit, which enables us, for the first time, to construct a set of templates that closely resemble predictions from numerical simulations. In this study, we investigate the possibility of detecting gravitational waves from core-collapse supernovae using a matched-filtering methods. We construct a theoretically-informed template bank and use it to recover a core-collapse supernova signal injected into real LIGO-Virgo-KAGRA detector data. We evaluate the detection efficiency of the matched-filtering approach and how well the injected signal is reconstructed. We discuss the false alarm rate of our approach and investigate the main source of false triggers. We recover 88% of the signals injected at a distance of 1 kpc and 50% of the signals injected at 2 kpc. For more than 50% of the recovered events, the underlying signal characteristics are reconstructed within an error of 15%. We discuss the strengths and limitations of this approach and identify areas for further improvements to advance the potential of matched filtering for supernova gravitational-wave detection. We also present the open-source Python package SYNTHGRAV used to generate the template bank.

Key words: gravitational waves – supernovae: general – methods: data analysis

1 INTRODUCTION

Core-collapse supernovae are among the most energetic events in the universe, producing gravitational waves (GWs) from asymmetric mass motions and neutrino emissions during the explosion. These GW signals offer a unique opportunity to probe the physics of core-collapse supernovae and their outcome. It is challenging to detect GWs from core-collapse supernovae because of their typically low amplitudes and highly stochastic nature, which are difficult to isolate within the noisy data streams of GW detectors like the LIGO, Virgo, and KAGRA interferometers. As a result, traditional GW detection efforts for supernovae have relied on excess energy searches, which identify broad-band signals without specific waveform models, in contrast to the matched-filtering approach that has been successfully applied to binary coalescences (see for example [Abbott et al. \(2023a\)](#)). Matched filtering has traditionally not been used for core-collapse supernovae due to the irregular, noise-like quality of the signals. Supernova GWs lack the clean structure of binary mergers, instead displaying complex broad-band emission. Consequently, detection studies primarily rely on excess energy methods ([Arnaud et al. 2004](#); [Ando et al. 2005](#); [Yokozawa et al. 2015](#); [Hayama et al. 2015](#); [Gossan et al. 2016](#); [Abbott et al. 2016](#); [Srivastava et al. 2019](#); [Abbott et al. 2020](#); [Halim et al. 2021](#); [Szczepańczyk et al. 2021](#); [Abbott](#)

[et al. 2021](#); [Richardson et al. 2022](#); [Afle et al. 2023](#); [Szczepańczyk et al. 2023](#); [Bruel et al. 2023](#); [Szczepańczyk et al. 2024](#); [Gill 2024](#)), Bayesian analysis and/or principle component analysis ([Summerscales et al. 2008](#); [Powell et al. 2016, 2017](#); [Powell 2018](#); [Roma et al. 2019](#); [Afle & Brown 2021](#); [Powell & Müller 2022](#); [Raza et al. 2022](#)), and machine learning techniques ([Astone et al. 2018](#); [Chan et al. 2020](#); [López et al. 2021](#); [Mukherjee et al. 2021](#); [Antelis et al. 2022](#); [Mitra et al. 2023](#); [Casallas-Lagos et al. 2023](#)).

However, recently matched-filtering techniques have seen some limited application for core-collapse GWs. [Drago et al. \(2023\)](#) investigated the possibility of exploiting the fact that the standing accretion shock instability (SASI) creates similar modulations in both the neutrino ([Tamborra et al. 2013](#)) and the GW signals ([Andresen et al. 2017](#)). By using the neutrino signal to construct a filter for the GWs, [Drago et al. \(2023\)](#) reported improved detection efficiencies for nearby events over standard excess energy methods. [Richardson et al. \(2024\)](#) demonstrated that matched-filtering methods are very promising for the secular GW emission from core-collapse supernovae associated with asymmetric emission of neutrinos and aspherical matter ejection (see, for example, [Epstein \(1978\)](#); [Turner \(1978\)](#); [Mueller & Janka \(1997\)](#); [Richardson et al. \(2022\)](#)).

Theoretical advancements in modelling core-collapse supernovae and their associated GW signals have provided a clearer understanding of the expected features of these GW signals. Multi-dimensional simulations have revealed supernova GWs consist of several complex

* E-mail: haakon.andresen@astro.su.se

signal components (Kotake et al. 2009; Murphy et al. 2009; Marek et al. 2009; Scheidegger et al. 2010; Yakunin et al. 2010; Kotake et al. 2011; Müller et al. 2012, 2013; Cerdá-Durán et al. 2013; Kuroda et al. 2014; Yakunin et al. 2015; Kuroda et al. 2016; Andresen et al. 2017; Kuroda et al. 2017; Takiwaki & Kotake 2018; Hayama et al. 2018; Morozova et al. 2018; O’Connor & Couch 2018; Radice et al. 2019; Andresen et al. 2019; Powell & Müller 2019, 2020; Shibagaki et al. 2020; Mezzacappa et al. 2020; Zha et al. 2020; Vartanyan & Burrows 2020; Andresen et al. 2021; Pan et al. 2021; Takiwaki et al. 2021; Eggenberger Andersen et al. 2021; Raynaud et al. 2022; Vartanyan et al. 2022; Jardine et al. 2022; Mezzacappa et al. 2023; Bugli et al. 2023; Vartanyan et al. 2023; Powell et al. 2023; Jakobus et al. 2023; Pajkos et al. 2023; Andresen et al. 2024; Choi et al. 2024). Each component is characterized by a time-dependent central frequency, with GWs emitted around this frequency. In addition to the main signal components, the signals show broadband background emission, sometimes called the “haze” (Vartanyan et al. 2023).

The theoretical understanding of individual emission components, developed through direct analysis of numerical simulations and studies of supernova oscillation modes (Murphy et al. 2009; Müller et al. 2013; Fuller et al. 2015; Sotani & Takiwaki 2016; Torres-Forné et al. 2018; Morozova et al. 2018; Torres-Forné et al. 2019a,b; Sotani et al. 2019, 2021; Andresen et al. 2021; Rodríguez et al. 2023; Wolfe et al. 2023; Zha et al. 2024), enables the construction of template banks guided by theoretical predictions. If these template banks can sufficiently capture the range of possible core-collapse supernova signals, matched-filtering methods may become applicable to supernova GW detection.

This study explores the feasibility of a template-based approach by recovering a supernova signal injected into LIGO-Virgo-Kagra (LVK) detector data. Our goal is to assess the performance of a simple matched template approach using a relatively small template bank in terms of detection efficiency, signal reconstruction, and false alarm rate (FAR). Additionally, we identify potential extensions of our techniques to achieve further improvement.

This paper is structured as follows. In Section 2, we describe the GW signal we inject (Subsection 2.1), the matched-filtering process (Subsection 2.2), and the template bank (Subsection 2.3). We give a detailed description of the Python package SYNTHGRAV used to generate the templates (Subsection 2.4). In Section 3, we consider an optimal detection scenario to establish a baseline for performance. We present the result of our matched-filtering approach in Section 4, evaluating detection efficiency, signal reconstruction, and related metrics. We address the challenge of false alarms in Section 5 and conclude in Section 6, where we discuss the implications of our findings and potential avenues for further refinement of supernova GW detection methods.

2 METHODS

2.1 Gravitational-Wave Signal

Several GW signal predictions from three-dimensional core-collapse supernova models exist in the literature. While the input physics impacts the results of numerical simulations, the signal predictions of recent simulations are converging. As a representative model, we choose a recent supernova simulation performed with the CHIMERA code (Bruenn et al. 2020). The simulation is based on a non-rotating progenitor with solar metallicity and a zero-age main sequence mass of 25 solar masses (Mezzacappa et al. 2023). We follow the naming convention of the CHIMERA models and label the model “D25” (D

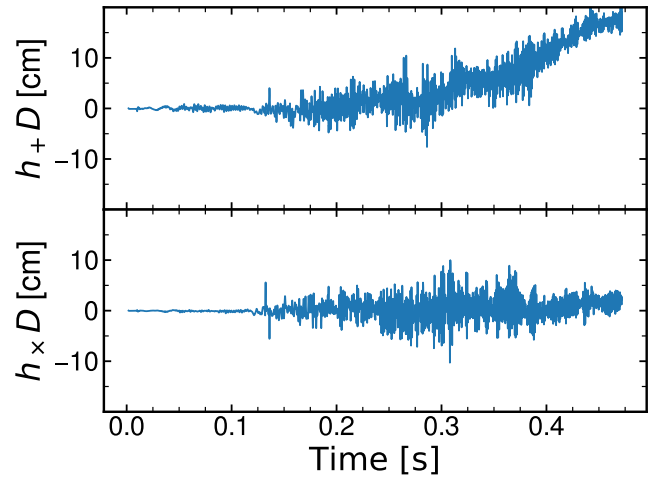


Figure 1. The plus (top) and cross (bottom) polarisation components of the GW signal from D25, for an observer located in the direction $(\phi, \theta) = (35^\circ, 0^\circ)$ in a spherical coordinate system centred on the simulation. Time is given in seconds after bounce. We show hD , where D is the distance to the source.

stands for the D-series of CHIMERA models). Rapid shock expansion sets in at approximately 250 ms after bounce in the D25 model.

The GW signal for an observer at $(\phi, \theta) = (35^\circ, 0^\circ)$ in a spherical coordinate system centred on the simulation is shown in Fig. 1. We plot the two independent components of the GW tensor in the transverse-traceless gauge. The top panel shows the plus polarisation mode (h_+) and the bottom panel shows the cross polarisation mode (h_\times). Time is given in seconds after core bounce. The plot shows the combined signal from asymmetric matter motions and neutrino emissions, with the GW strain scaled by the distance to the source. The signal is comprised of two distinct components: a high-frequency, stochastic component with an amplitude between 5 and 10 cm, and a slower-evolving component that emerges later in the simulation, reaching amplitudes up to 20 cm. This second component, the linear memory, arises from the aspherical expansion of the shock and asymmetric neutrino emissions. This work focuses on the first component, which is generated by turbulence in and around the forming neutron star. In Fig. 2, we show the spectrogram of the signal. We compute the spectrogram by applying short-time Fourier transforms (STFT) to h_+ and h_\times individually before taking the square sum of the two resulting STFTs. The STFTs are computed with a SCIPY.SIGNAL.STFT using a Blackman window (Virtanen et al. 2020). We normalize the STFTs and take the base 10 logarithm before plotting. The normalization is chosen so that the logarithmic value lies within $(-\infty, 0]$. Before computing spectrograms, we filter the signals using high-pass and low-pass filters to remove any part of the signal below 25 Hz or above 2500 Hz. The typical signature of GWs from supernovae is visible in Fig. 2, with the main emission component appearing around ~ 0.1 s and its central frequency increasing more or less linearly over time. The dashed white line in Fig. 2 shows the straight line given by $y = 2700t + 100$ and guides the eye towards the central frequency of the GW signal. The solid white line shows the central frequency of a particular template, which we will return to in Section 4. While the strain versus time looks stochastic and noisy at first glance, there is clearly structure in the time-frequency domain. It is this structure that forms the basis of the templates we use in this work. In addition to the emission seen in Fig. 2, several other signal

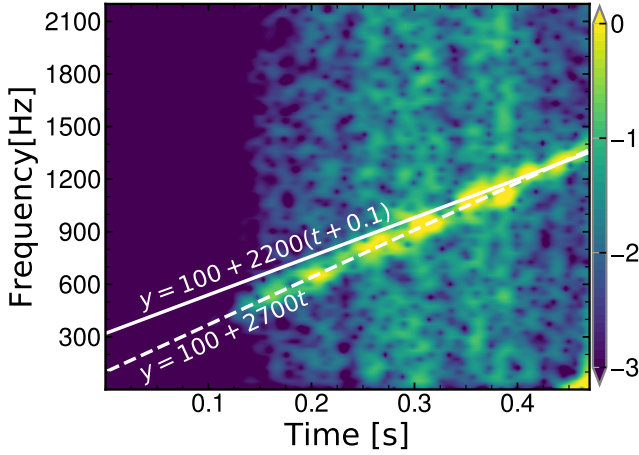


Figure 2. Spectrogram of the GW signal emitted by model D25. The colour scale is logarithmic and the Fourier amplitudes have been normalised to lie within $(-\infty, 0]$. The dashed white line illustrates the linear growth of the central frequency of the signal. The solid white line represents the frequency evolution of the most commonly reconstructed template (see Section 4.2). Time is given in seconds after core bounce.

components can emerge in GW emission from core-collapse supernovae. For example, if strong SASI activity develops, it will lead to narrowband emission centred around 100 Hz (Kuroda et al. 2016; Andresen et al. 2017). However, the D25 model does not exhibit vigorous SASI activity.

2.2 Noise Injection and Matched Filtering

We inject the signal into an approximately week-long stretch of O3b LIGO-Virgo-KAGRA (LVK) data, between GPS time 1266368512 and 1267063808, obtained from the Gravitational Wave Open Science Center (GWOSC) (Abbott et al. 2023b). During the analysis, we consider only data frames without holes or other quality issues, which provides us with 3.41 days of usable data. Some of the smaller data quality issues we encountered, such as small stretches of missing data, can most likely be fixed with standard techniques.

We consider a two-detector network consisting of the Livingston and Hanford LIGO detectors. We do not include the Virgo detector in our analysis because it is more challenging to find periods where all three detectors were online, and we do not see a significant improvement when including three detectors. We refer the reader to Szczepańczyk et al. (2021) for a discussion regarding detector networks and their importance for core-collapse supernovae.

The data from GWOSC is divided into 4096 s long frames, and we inject the signal once per data frame at random sky locations. We obtain the data through the GWOSC Python interface (Abbott et al. 2023b). We then use GWPY (MacLeod et al. 2021) to project, whiten, and inject the signals into the data stream. The whitening in GWPY uses inverse spectrum truncation. We perform the matched filtering using the functionality of PYCBC (Allen 2005; Allen et al. 2012; Dal Canton et al. 2014; Nitz et al. 2017, 2024). We repeat the analysis three times for three different injection distances: 1 kpc, 2 kpc, and 5 kpc.

After injecting the signal into the data frames, we calculate the matched-filtering signal-to-noise ratio (SNR) using functionality from PYCBC, with an upper-frequency cut-off of 2000 Hz. We use a template bank of 150 templates, see Section 2.3 for details. In the

matched filtering, we estimate the PSD of the noise using the whole data frame. We cluster the resulting SNR values into 1 s long segments and set the SNR of a bin to the maximum value within that bin. We choose the duration of our bins based on the fact that the length of the signal is less than half a second. We calculate the SNR of each template in both detectors and define the network SNR as

$$SNR_n^2 = SNR_L \cdot SNR_H, \quad (1)$$

where SNR_L and SNR_H represent the SNR values in the Livingston and Hanford detectors, respectively. We consider a trigger as an event with a SNR_n larger than six. Sometimes, holes in the data or issues during the SNR calculation resulted in corrupted SNR data values. We only consider those frames where the two LIGO detectors returned usable SNR values; in effect, we only consider frames with two detector coverage.

2.3 Signal Templates

We generate a set of 150 templates with the newly developed SYNTHGRAV Python package, see Section 2.4. The templates are constructed in such a way that the central frequency (f_c) of the templates evolves linearly with time (t), in other words, $f_c(t) = at + b$. We choose three different b values for the sample: 100 Hz, 200 Hz, and 300 Hz. The more interesting parameter, the slope of the frequency evolution, is sampled in 50 equidistant steps from 250 Hz/s to 3000 Hz/s. For simplicity, we will omit the units of a and b going forward.

The way we generate templates does not inherently include any information about the signal amplitude as a function of time, but it can and should be included in the template generation. In principle, one should add the time evolution of the amplitude as a free parameter in the template bank. Doing so, however, increases the size of the template bank and the computational cost of the matched filtering. Here, as a first step, we circumvent this by extracting an envelope from the signal we inject and using the envelope to determine the time dependence of the template amplitude. We extract the envelope using the Hilbert transformation from SCIPY.SIGNAL.HILBERT and we smoothen the envelope using a third order Savitzky–Golay filter (using SCIPY.SIGNAL.SAVGOL_FILTER).

We show one example of our templates in Fig. 3: the blue lines represent the template (after multiplying with the envelope), the grey outlines represent the actual signal, and the red lines show the envelope extracted from the signal. Fig. 4 shows the spectrogram of the template in Fig. 3. We see that the template mimics the main component of the real signal, but that the shape of the background noise of the template differs from the background emission in Fig. 2. The white line in Fig. 4 represents the central frequency curve used to construct the template.

2.4 SynthGrav

In SYNTHGRAV, a GW signal is constructed from a set of modes. Each mode is characterised by a time-dependent central frequency f_c . The polarisation of each mode is determined individually and the signal is constructed as a weighted sum of modes

$$h_{\times/+}(t) = \sum_i w_{\times/+}^i(t) A_{\times/+}^i(t), \quad (2)$$

where the $w_{\times/+}^i(t)$ indicate time-dependent weight functions and the $A_{\times/+}^i(t)$ denote the time-dependent amplitudes of the i -th mode. When the final signal has been assembled as the sum of the individual

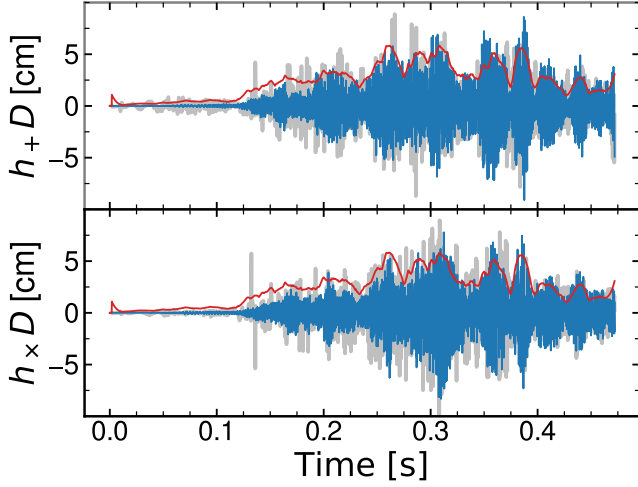


Figure 3. The blue curve shows an example template, the grey curve shows the injected signal for comparison, and the red line shows the envelope extracted from the signal which we used to set the time evolution of the template amplitude. Time is given in seconds after bounce. The top panel shows the plus polarisation mode and the bottom panel shows the cross polarisation. Both strain values have been multiplied by the distance (D) to the source.

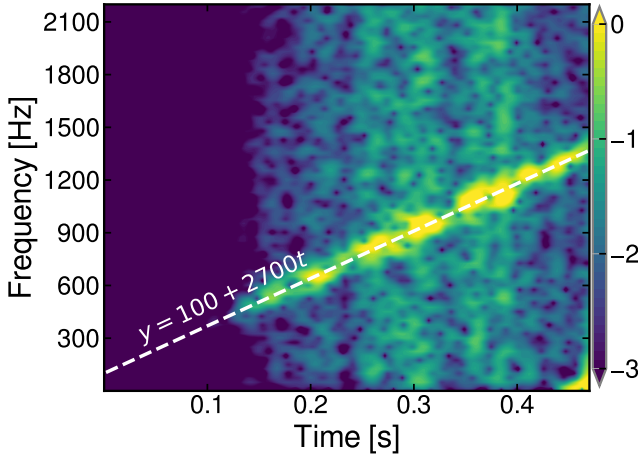


Figure 4. Spectrogram of an example template, with the white dashed line illustrating the central frequency evolution used to construct the template. The colour bar shows the logarithmic amplitude scale.

modes, it is possible to apply a global time-dependent weight to the total signal, which we will refer to as an envelope.

Each mode is constructed from a series of overlapping pulses, each consisting of coloured random noise. For a pulse centred at t^j , we first define the central frequency $f_c^j = f_c(t^j)$. A sequence of random numbers is then generated from a uniform distribution, denoted as H_{white} , with its Fourier Transform given by \tilde{H}_{white} . The subscript “white” highlights that these random numbers represent uncoloured white noise. To colour the noise, we have to choose the normalised power spectral density (PSD) of the coloured noise. First, we choose a function $S(f, f_c^j)$ centred around f_c . By default we use a Gaussian for $S(f, f_c^j)$, but the user can freely specify $S(f, f_c^j)$ and the software comes with a few predefined options (see the documentation accompanying the software). The normalised PSD

is then defined as follows

$$S_{\text{norm}}(f, f_c) = S(f, f_c^j) / \sqrt{\langle S(f, f_c^j)^2 \rangle}, \quad (3)$$

where $\langle S(f, f_c^j)^2 \rangle$ denotes the mean of $S(f, f_c^j)^2$. The white noise is then weighted by the normalised PSD. This is done by multiplying the normalised PSD with the Fourier transform of the white noise H_{white} in the frequency domain, which defines

$$\tilde{H}_{\text{shaped}} = \tilde{H}_{\text{white}} \cdot S_{\text{norm}}(f). \quad (4)$$

Lastly, the shaped noise is converted back into the time domain by performing an inverse Fourier transform on $\tilde{H}_{\text{shaped}}$. We add the pulses together to generate the mode in question. Depending on the choice of polarisation, the process is repeated for the plus and cross components of h .

The user can freely determine the central frequency of each mode, but SYNTHGRAV comes with a set of supernova-specific modes based on the fitting formulas of Torres-Forné et al. (2019a).

The code is publicly available at <https://github.com/haakoan/SynthGrav>. We refer the reader to the accompanying documentation for a more in-depth explanation of the code’s functionality.

3 AN OPTIMAL SCENARIO

In general, the matched-filtering SNR for some filter $K(t)$ is given by

$$SNR = \frac{\int \tilde{h}(f) \tilde{K}^*(f) df}{\left(\int \frac{1}{2} S_n(f) |\tilde{K}(f)|^2 df \right)^{1/2}}, \quad (5)$$

where $S_n(f)$ denotes the noise spectral density and $\tilde{K}^*(f)$ is the complex complex conjugate of $\tilde{K}(f)$, which is the Fourier transform of $K(t)$. The Fourier transform of the signal $h(t)$ is represented by \tilde{h} . As is well-known in the GW astronomy literature, the filter which maximises Eq. 5 is the signal itself, see Maggiore (2007) for a detailed derivation and discussion.

The combination of semi-analytical methods and numerical simulations has allowed for the creation of large template banks for compact binary merger signals. The template banks used to detect compact binary mergers are almost complete in large parts of the parameter space and contain templates that are almost perfect matches to the observed signals. This is, in practice, only possible because the signals from inspiraling binaries are relatively simple: they look like chirp signals that grow louder the closer to merger the binaries get. The stochastic and noisy GW signals expected from core-collapse supernovae are diametrically opposite to the signals from compact binary mergers.

It will never be possible to create complete template banks for core-collapse supernova signals, but the matched-filtering SNR assuming optimally-orientated detectors is commonly reported in the literature because it provides a relatively easy way to gauge the detectability of signal predictions from numerical simulations (see, for example, the discussion in Andresen et al. (2017)). Following this idea, we investigate how well matched filtering would perform under the assumption of a perfect signal prediction and opportune detector orientations (relative to the source). This analysis places an upper bound on the methodology presented in this paper.

We choose the data frames with a starting GPS time 1266450432 and inject the signal into the data after 2100 s. We then perform matched filtering with the signal as the filter; the resulting SNR_n is

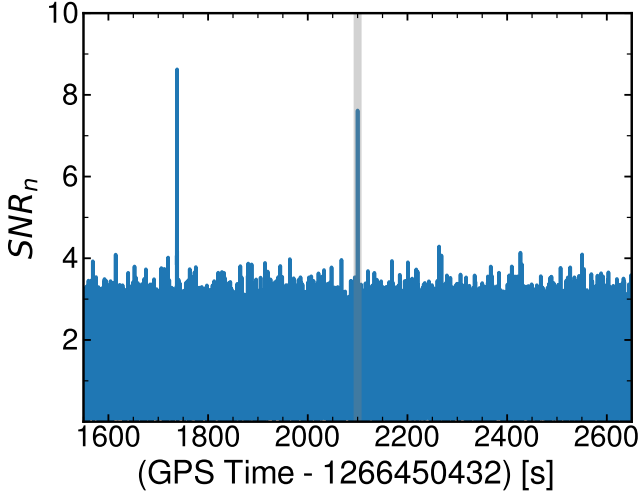


Figure 5. Network SNR for an event at 10 kpc using the signal itself as the filter. The signal was injected 2100 s into the data frames starting at GPS time 1266450432. The shaded grey vertical region indicates the injection time.

shown in Fig. 5. The signal was injected at the sky location (right ascension, declination) = (24 h, 35°), with a polarisation angle of zero, and assuming a source distance of 10 kpc. The shaded grey region in Fig. 5 highlights the injection time. The injected signal is visible with a $SNR_n > 6$, but a false trigger is also visible (the peak between 1600 and 1800 s). We return to false alarms in Section 5. The SNR_n depends on the observer orientation. Sampling 25 evenly spaced observers around the simulated supernova, we found a mean SNR_n value of 6.2, a maximum value of 7.5, and a minimum value of 4.2.

Clearly, matched filtering effectively detects supernova signals in current interferometers for a source within the Milky Way under the right conditions. The critical question is how well our template bank will perform compared to the optimal scenario.

4 DETECTING AND RECONSTRUCTING THE SIGNAL USING A TEMPLATE BANK

4.1 Detecting Events

We now turn our attention to the realistic scenario in which we do not know the exact supernova signal. Instead, we rely on an underlying theoretical understanding of core-collapse supernova GWs that we use to construct a template bank.

The detection efficiencies for three distances, 1 kpc, 2 kpc, and 5 kpc, and a SNR_n threshold of 6 are shown in Fig. 6. Our choice of threshold can be understood from Fig. 5; the correlation of the signal with pure detector noise leads to an ambient SNR of $\sim 3 - 4$, so a threshold of 6 lies well above this background. However, based on Fig. 5 we expect to pick up several false triggers with a threshold of 6. We recover 88% of the injected signals at 1 kpc. Doubling the distance reduces the detection efficiency to $\sim 50\%$, and we do not recover any of the signals injected at 5 kpc. Our method performs well in comparison to state-of-the-art excess energy searches, but the comparison is not straightforward. First, excess energy searches typically implement better glitch vetoing (we do not veto any glitches). Second, recent studies have focused on the performance of excess energy methods for the fourth and fifth LVK

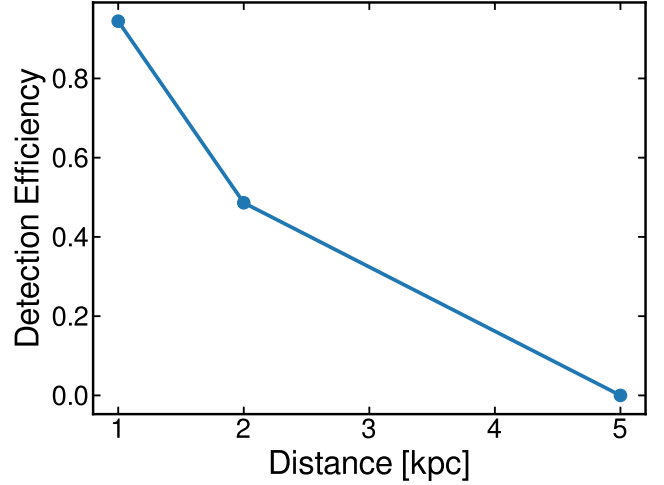


Figure 6. Detection efficiency as a function of source distance, showing results for injections at distances of 1, 2, and 5 kpc (marked by the blue dots) with a network SNR threshold of 6.

observation runs (Szczepańczyk et al. 2021), for which the noise floor is expected to be reduced by a factor between two and five (LIGO Scientific Collaboration 2022). Still, comparing our results to Fig. 7 of Szczepańczyk et al. (2021) we see similar detection efficiencies, but the excess energy approach performs slightly better than our method and reaches detection efficiencies of 60% out to 3 – 10 kpc for similar waveforms to the one used in this study (they inject a set of signal predictions). However, it is unclear how large a role the differences in the noise used in Szczepańczyk et al. (2021) and the noise we use effects the comparison. Comparing our result to Szczepańczyk et al. (2023), we see that our matched-filtering method outperforms the excess energy search by almost a factor of 10 (see their Fig. 4). A direct comparison to Szczepańczyk et al. (2023) is not straight forward because they enforce a FAR of one per hundred years, whereas we do not consider false alarms when calculating the detection efficiency (see Section 5 for a discussion regarding our FAR). For galactic events, the blind search methodology employed by the LVK is not the most efficient approach, and the FAR can be significantly reduced by incorporating timing information from neutrino detectors. Szczepańczyk et al. (2024) performed an optically triggered search for core-collapse supernovae during the third LVK observation run and report detection efficiencies similar to what we find. Waveforms similar to the one used in this work are detected with an efficiency of 50% at 2 kpc, see Fig. 6 of Szczepańczyk et al. (2024). However, it is not clear what the authors assume about the FAR when reporting the detection efficiency.

A proper comparison of excess energy methods and matched filtering requires controlling the FAR, injecting the same signals, and using the same detector noise. With this in mind, the method proposed in this work performs relatively well compared to excess energy methods. Furthermore, our approach can likely be refined to achieve improved detection efficiencies.

The detection efficiency depends on the orientation of the observer relative to the supernova explosion. To quantify the effect of observer orientation, we repeat the analysis from Section 3. Calculating SNR_n for 25 observers equally spaced in a spherical coordinate system centred on the simulation and a source at 1 kpc, we find a mean SNR_n of 7.0 and maximum and minimum values of 12.5 and 2.7, respectively. To judge the impact of our method to calculate the

envelope of the signal (see Section 2.3), we perform the same analysis without including the envelope when constructing the templates. Without the envelope, we find an overall reduction in SNR_n . The mean, maximum, and minimum SNR_n values are reduced to 6.3, 10.7, and 1.7, respectively. This shows that the envelope is not critical to our analysis, but that including the envelope increases the SNR_n by $\sim 10\%$. Furthermore, the GWs from a supernova might not be detectable for every observer. On the other hand, the fact that SNR_n shows a smaller variation for the optimal scenario indicates that the method explored in this work has room to be improved.

4.2 Reconstructing the Signal

The reconstructed signal is defined as the template that yields the highest SNR_n . We show the distribution of reconstructed a and b values (the input parameters of our templates) in Fig. 7. The left panel of Fig. 7 corresponds to an injection distance of 1 kpc and the right panel shows the results for signals injected at a distance of 2 kpc. The blue bars in the main plot show the reconstructed a values and the green bars in the inset represent the reconstructed b values. For both the main panels and the insets, the y -axis gives the relative frequency of a reconstructed value, defined as the number of events reconstructed with a given parameter divided by the total number of recovered events. For both distances, we see from Fig. 7 that the majority of events are reconstructed with an a -value around 2250: close to 60% of the events at 1 kpc and around 35% of the events at 2 kpc. A b -value of 100 is reconstructed in more than 50% of the cases for both distances. From Fig. 2, we estimate the true slope of the high-frequency component of the signal to be approximately 2700 Hz/s. Therefore, our method underestimates the true value of the slope by at least 450 or roughly 15%. Casallas-Lagos et al. (2023) used machine learning techniques to recover the time-frequency evolution of signals injected at galactic distances and reconstructed GW bursts using the excess energy pipeline COHERENT WAVEBURST (Klimenko et al. 2016, 2021). The errors (for example, the standard deviation) reported by Casallas-Lagos et al. (2023) are similar to the errors reported in this work. However, Casallas-Lagos et al. (2023) studied a larger set of signals and their reported errors depended on the signal in question.

The reason why some events are misclassified is likely a combination of the noise characteristic at the exact time of injection and the similarity of the templates. The way we cluster SNR values that lie within our 1 s segments may also contribute. For the latter, we set the largest SNR value within a 1 s window as the window's SNR. A more robust method for clustering individual SNR peaks within the windows could impact the estimated SNR, but it also runs the risk of boosting the SNR artificially. Using shorter time segments to estimate the PSD of the noise, rather than the full 4096 s covered by individual frame files, should provide a better estimate of the properties of the noise around the injection. Finally, there is some inherent overlap in the templates. The dashed white line in Fig. 2 shows the true frequency evolution of the signal and the solid line shows the frequency evolution of a template with $a = 2200$ shifted 0.1 s forward in time. Visually, we see a good overlap between the frequency characteristics of the solid white line and the true signal. Since the templates include an initial quiescent phase lasting around 0.1 s, the shifted template has a very low amplitude between 0.1 s and 0.2 s. While the D25 model emits GWs during the first 0.2 s post bounce, the emission is stronger between 0.2 and 0.4 s post bounce. In Fig. 2, bursts of GW emission are clearly visible at ~ 0.3 s and ~ 0.4 s post bounce. The central frequency of the template overlaps well with the central frequency of the signal between 0.25 and 0.4

s. Consequently, one possible explanation for why the template with $a \sim 2200$ results in the highest SNR_n value is that the central frequency of the template and the signal overlaps well during periods when the signal is strong, when the template is shifted forward in time by 0.1 s relative to the start of the signal.

Reconstructing the central value of the main signal component and its slope is particularly interesting for core-collapse signals because it is set by the properties of the proto-neutron star (PNS). It has been shown that the central frequency of the emission can be expressed as

$$f_{\text{GW}} = \frac{1}{2\pi} \frac{GM_{\text{PNS}}}{R_{\text{PNS}}^2} \sqrt{1.1 \frac{m_n}{\langle \epsilon_{\bar{\nu}} \rangle}} \left[1 - \frac{GM_{\text{PNS}}}{R_{\text{PNS}} c^2} \right]^2, \quad (6)$$

where M_{PNS} is the mass of the PNS, R_{PNS} is the radius of the PNS, $\epsilon_{\bar{\nu}}$ is the average anti-electron neutrino energy (Müller et al. 2013). The constants in m_n , c , and G are the neutron rest mass, the speed of light, and Newton's constant, respectively. The average energy of anti-electron neutrinos can be measured from neutrino observations, which leaves two unknowns: the mass and radius of the PNS. Together, the PNS mass and PNS radius determine the compactness of the PNS, which is a measure of the properties of the underlying equation of state.

5 FALSE ALARMS

So far, we have not considered the FAR in our discussion of our results. It is clear from Fig. 5 that a network SNR threshold of 6 will lead to false triggers. In Fig. 8, we show the FAR as a function of the number of templates included in our analysis. The results represent signals injected at a source distance of 1 kpc. Using the full template bank (with 150 templates), we find a FAR of ~ 130 per day. We also see that while the FAR grows nonlinearly with the number of templates, there is a relatively small difference, roughly 15%, in the FAR when using five and 150 templates. The difference in the FAR between 50 and 150 templates is approximately 8%. We do not show the FAR as a function of distance, but it does not change much when changing the injection distance, which is what we would expect for false triggers.

A FAR of 130 events means the matched-filtering method presented in this work is not yet suited to run as a stand-alone and independent search. However, core-collapse supernovae are true multi-messenger events, and we expect that neutrino detectors will pin down the time of the explosion with millisecond precision for a galactic event (Azfar et al. 2024). With a FAR of 130, the probability of a false trigger randomly aligning with a neutrino detection is $\sim 1 \times 10^{-3}$, if we divide the data into 1 s long segments.

Furthermore, most of the false triggers occur within 1 s from a noise glitch. We show three examples of the glitches that produce false alarms in our analysis in Fig. 9. A smaller number of false triggers cannot be associated with glitches. We did not attempt to veto glitches or perform a detailed noise study with the specifics of core-collapse signals in mind. Our FAR can likely be reduced significantly by using existing methods for detecting and removing glitches (Bondaescu et al. 2023; Tolley et al. 2023). Beyond removing obvious glitches, a detailed detector characterisation targeted at core-collapse supernovae will be necessary to understand the true FAR. We leave a more detailed treatment of glitches for future work.

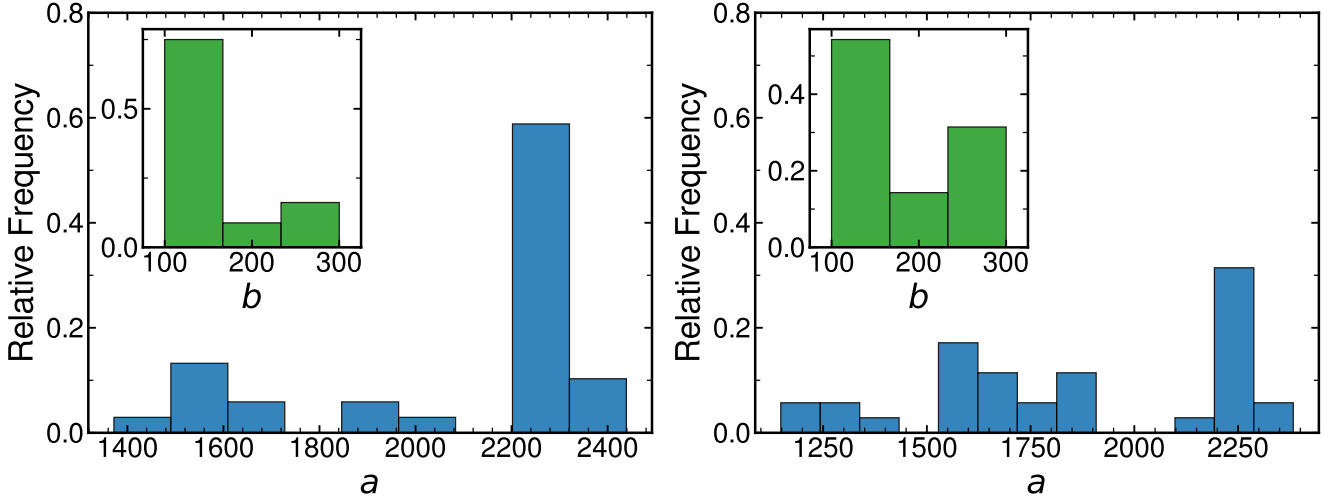


Figure 7. Distribution of reconstructed parameters (a and b values) for template matching at 1 kpc (left) and 2 kpc (right). Blue bars represent reconstructed a -values, while green bars in the inset show reconstructed b -values. The parameter b is given in Hz and a is in Hz/s.

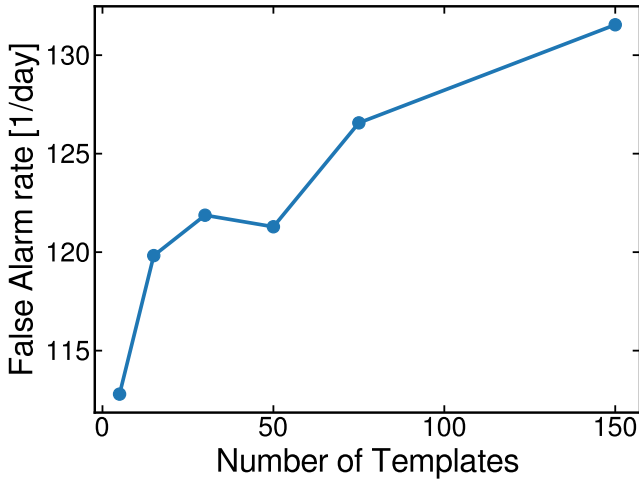


Figure 8. FAR as a function of the number of templates in the template bank. The blue dots represent actual data points.

6 CONCLUSIONS

In this work, we explored the feasibility of detecting GWs from core-collapse supernovae through matched filtering, using signal injections into data from the LVK O3b run. Using the newly developed template generation code `SYNTHGRAV`, we constructed a template bank of synthetic core-collapse supernova GW signals. `SYNTHGRAV` is specifically designed to match the frequency characteristics observed in core-collapse supernova signals. Crucially, while the synthetic signals do not match the injected signal perfectly, the overall morphology of the templates resembles the injected signal well enough to enable the use of matched-filtering methods.

We studied the detectability of one signal from a simulation of the core collapse of a solar-metallicity star with a zero-age main sequence mass of 25 solar masses. Under optimal conditions and using the signal itself as the template, this signal is detectable with a network SNR above 6 at 10 kpc. Using a template bank consisting of 150 templates constructed with `SYNTHGRAV`, we found a detection

efficiency of $\sim 88\%$ at a distance of 1 kpc and $\sim 50\%$ at 2 kpc. No signals were detected at a distance of 5 kpc. In the majority of the cases, we found that the properties of the signal, the typical frequency of the signal as a function of time, can be reconstructed with an accuracy of $\sim 15\%$.

We found a relatively large variation in our results as a function of observer direction, a SNR_n change of approximately 80%. For the optimal scenario, where the signal itself was used as the filter, we saw a smaller variation in SNR_n ($\sim 40\%$).

Our study demonstrates that matched-filtering methods perform relatively well in comparison with state-of-the-art excess energy searches (Szczepańczyk et al. 2021, 2023, 2024).

We found that the FAR was primarily driven by noise glitches, resulting in a relatively high FAR that underscores the importance of incorporating glitch-rejection techniques into the analysis. Additionally, improving our understanding of the correlation between the detector data stream and supernova signals could help reduce the FAR further. However, since neutrino detections would likely accompany a galactic supernova, we can tolerate a higher FAR than is typically acceptable in blind searches for compact binary merger signals. Consequently, we can prioritise sensitivity to supernova signals over reducing the FAR, with the expectation that neutrino observations will aid in confirming an actual event.

Looking to the future, to improve the accuracy of the method proposed in this paper, we propose the following advancements.

(i) Improving the template bank: Developing a more comprehensive template bank that includes a broader spectrum of possible supernova signals would improve detection prospects, especially for progenitors exhibiting additional signal components (such as emission due to SASI activity). Furthermore, the simple linear central-frequency evolution of the main signal component should be replaced with a more realistic functional form. Torres-Forné et al. (2019a) derived a set of polynomial expressions that link the central frequencies of various modes to the underlying physical properties of the supernova core. Their prescription is implemented in `SYNTHGRAV` and can in the future be used to generate more sophisticated templates.

(ii) Glitch rejection: Addressing the high FAR requires advanced glitch rejection methods and supernova-specific detector characterisation (see Magee et al. (2024) and Smith et al. (2024) for recent

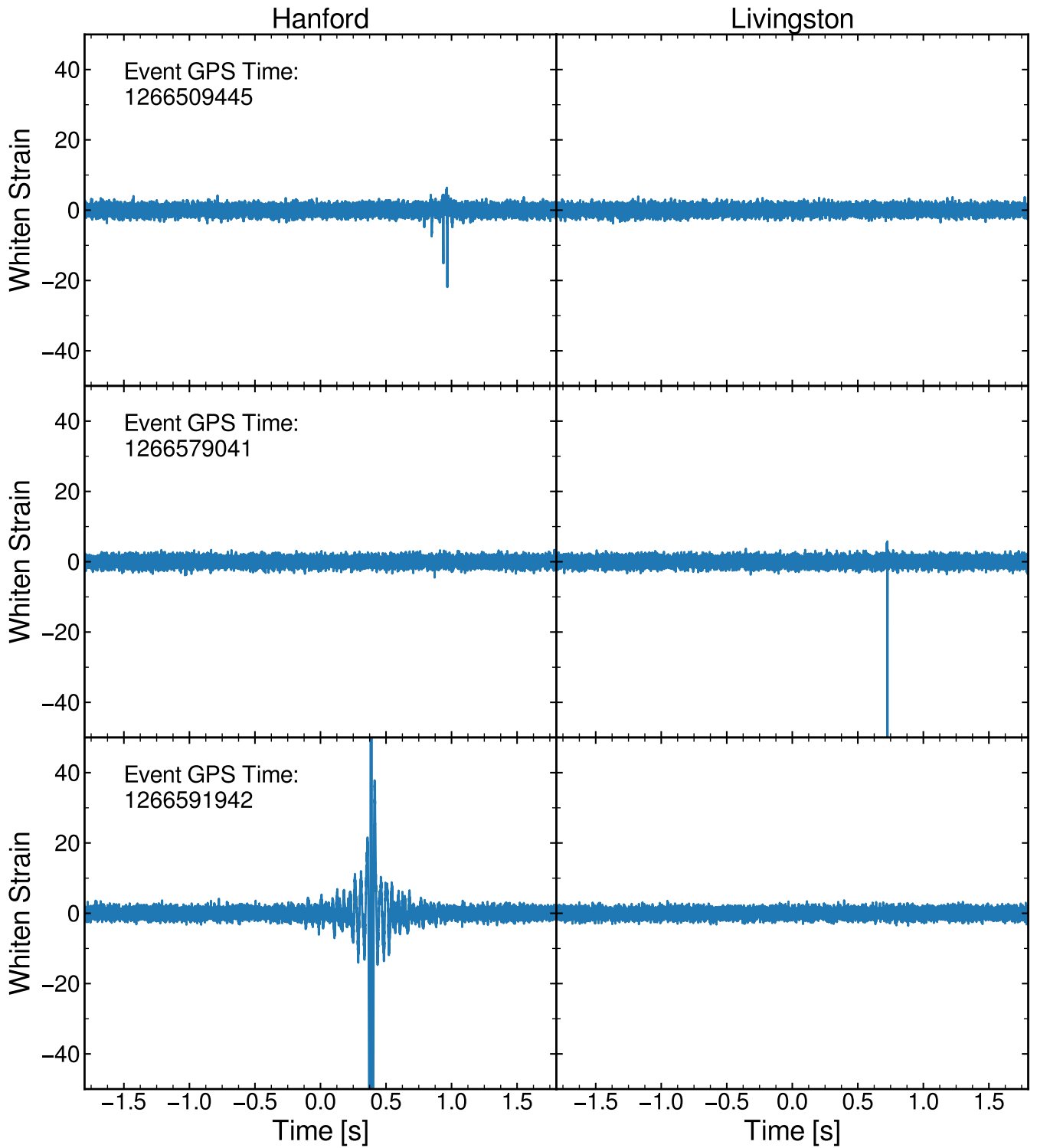


Figure 9. Examples of noise glitches that generated false alarms during the analysis. Each row displays a different noise glitch resulting in a false alarm. The GPS time for each event is indicated in the upper left corner of the left panel. The left column represents the data stream from Hanford. Data from Livingston are shown in the right column. The time axis for each panel is a 3 s wide window around the noise trigger. The data shown has been whitened using `GWPY.TIMESERIES.WHITEN()`.

examples of glitch removal techniques). In excess energy searches targeting core-collapse supernova signals, machine learning methods have proven effective at removing blip glitches, one of the most problematic types for supernova signal detection (Szczeptańczyk et al. 2023).

(iii) Refining the matched-filtering methodology: Optimising the matched-filtering process, for example, by improving PSD estimation in shorter time segments and clustering SNR peaks better, could improve the efficiency of the classification method.

Additionally, it will be necessary to inject a broader range of signals in the future and study the efficiency of our method as a function of the injected signal. In this work, we have focused on the primary GW signal component, often attributed to g-modes in the PNS (Andresen et al. 2017). However, other signal components, such as those associated with SASI activity (Kuroda et al. 2016; Andresen et al. 2017) or various PNS oscillation modes (Jakobus et al. 2023), are also observed in some cases. Understanding how well these different signal components can be detected and reconstructed is important for determining what we can infer about physical quantities, such as the compactness of the PNS or the evolution of the shock, from a future core-collapse supernova GW detection. With only a handful of theoretical signal predictions available in the literature, the ability to generate synthetic signals using SYNTHGRAV will improve our ability to study the detectability of different signal morphologies.

ACKNOWLEDGEMENTS

We thank Michele Zanolin for valuable feedback on the manuscript.

This work was enabled by resources provided by the National Academic Infrastructure for Supercomputing in Sweden (NAISS) and the Swedish National Infrastructure for Computing (SNIC) at NSC partially funded by the Swedish Research Council through grant agreements no. 2022-06725 and no. 2018-05973. This work is supported by the Swedish Research Council (Project No. 2020-00452).

This material is based upon work supported by the National Science Foundation Graduate Research Fellowship Program under Grant No. 2137424. Any opinions, findings, and conclusions or recommendations expressed in this material are those of the authors and do not necessarily reflect the views of the National Science Foundation. Support was also provided by the Graduate School and the Office of the Vice Chancellor for Research at the University of Wisconsin-Madison with funding from the Wisconsin Alumni Research Foundation.

This research has made use of data or software obtained from the Gravitational Wave Open Science Center (gwosc.org), a service of the LIGO Scientific Collaboration, the Virgo Collaboration, and KAGRA. This material is based upon work supported by NSF's LIGO Laboratory which is a major facility fully funded by the National Science Foundation, as well as the Science and Technology Facilities Council (STFC) of the United Kingdom, the Max-Planck-Society (MPS), and the State of Niedersachsen/Germany for support of the construction of Advanced LIGO and construction and operation of the GEO600 detector. Additional support for Advanced LIGO was provided by the Australian Research Council. Virgo is funded, through the European Gravitational Observatory (EGO), by the French Centre National de Recherche Scientifique (CNRS), the Italian Istituto Nazionale di Fisica Nucleare (INFN) and the Dutch Nikhef, with contributions by institutions from Belgium, Germany, Greece, Hungary, Ireland, Japan, Monaco, Poland, Portugal, Spain.

KAGRA is supported by Ministry of Education, Culture, Sports, Science and Technology (MEXT), Japan Society for the Promotion of Science (JSPS) in Japan; National Research Foundation (NRF) and Ministry of Science and ICT (MSIT) in Korea; Academia Sinica (AS) and National Science and Technology Council (NSTC) in Taiwan.

DATA AVAILABILITY

The data used in this study can be obtained from the Gravitational Wave Open Science Center. The signal we injected into the noise is publicly available. We will provide our Python scripts upon reasonable request.

REFERENCES

- Abbott B. P., et al., 2016, *Phys. Rev. D*, **94**, 102001
 Abbott B. P., et al., 2020, *Phys. Rev. D*, **101**, 084002
 Abbott R., et al., 2021, *Phys. Rev. D*, **104**, 122004
 Abbott R., et al., 2023a, *Physical Review X*, **13**, 041039
 Abbott R., et al., 2023b, *Astrophys. J. Suppl.*, **267**, 29
 Afle C., Brown D. A., 2021, *Phys. Rev. D*, **103**, 023005
 Afle C., Kundu S. K., Cammerino J., Coughlin E. R., Brown D. A., Vartanyan D., Burrows A., 2023, *Phys. Rev. D*, **107**, 123005
 Allen B., 2005, *Phys. Rev. D*, **71**, 062001
 Allen B., Anderson W. G., Brady P. R., Brown D. A., Creighton J. D. E., 2012, *Phys. Rev. D*, **85**, 122006
 Ando M., et al., 2005, *Phys. Rev. D*, **71**, 082002
 Andresen H., Müller B., Müller E., Janka H. T., 2017, *MNRAS*, **468**, 2032
 Andresen H., Müller E., Janka H. T., Summa A., Gill K., Zanolin M., 2019, *MNRAS*, **486**, 2238
 Andresen H., Glas R., Janka H. T., 2021, *MNRAS*, **503**, 3552
 Andresen H., O'Connor E. P., Andersen O. E., Couch S. M., 2024, *A&A*, **687**, A55
 Antelis J. M., Cavaglia M., Hansen T., Morales M. D., Moreno C., Mukherjee S., Szczeptańczyk M. J., Zanolin M., 2022, *Phys. Rev. D*, **105**, 084054
 Arnaud N., et al., 2004, *Astroparticle Physics*, **21**, 201
 Astone P., Cerdá-Durán P., Di Palma I., Drago M., Muciaccia F., Palomba C., Ricci F., 2018, *Phys. Rev. D*, **98**, 122002
 Azfar F., et al., 2024, *arXiv e-prints*, p. arXiv:2410.11984
 Bondarescu R., Lundgren A., Macas R., 2023, *Phys. Rev. D*, **108**, 122004
 Bruel T., et al., 2023, *Phys. Rev. D*, **107**, 083029
 Bruenn S. W., et al., 2020, *ApJS*, **248**, 11
 Bugli M., Guilet J., Foglizzo T., Obergaulinger M., 2023, *MNRAS*, **520**, 5622
 Casallas-Lagos A., Antelis J. M., Moreno C., Zanolin M., Mezzacappa A., Szczeptańczyk M. J., 2023, *Phys. Rev. D*, **108**, 084027
 Cerdá-Durán P., DeBrye N., Aloy M. A., Font J. A., Obergaulinger M., 2013, *ApJ*, **779**, L18
 Chan M. L., Heng I. S., Messenger C., 2020, *Phys. Rev. D*, **102**, 043022
 Choi L., Burrows A., Vartanyan D., 2024, *ApJ*, **975**, 12
 Dal Canton T., et al., 2014, *Phys. Rev. D*, **90**, 082004
 Drago M., Andresen H., Di Palma I., Tamborra I., Torres-Forné A., 2023, *Phys. Rev. D*, **108**, 103036
 Eggenberger Andersen O., Zha S., da Silva Schneider A., Betranhandy A., Couch S. M., O'Connor E. P., 2021, *ApJ*, **923**, 201
 Epstein R., 1978, *ApJ*, **223**, 1037
 Fuller J., Klion H., Abdikamalov E., Ott C. D., 2015, *MNRAS*, **450**, 414
 Gill K., 2024, *arXiv e-prints*, p. arXiv:2405.13211
 Gossan S. E., Sutton P., Stuver A., Zanolin M., Gill K., Ott C. D., 2016, *Phys. Rev. D*, **93**, 042002
 Halim O., Casentini C., Drago M., Fafone V., Scholberg K., Vigorito C. F., Pagliaroli G., 2021, *J. Cosmology Astropart. Phys.*, **2021**, 021
 Hayama K., Kuroda T., Kotake K., Takiwaki T., 2015, *Phys. Rev. D*, **92**, 122001
 Hayama K., Kuroda T., Kotake K., Takiwaki T., 2018, *MNRAS*, **477**, L96

- Jakobus P., Müller B., Heger A., Zha S., Powell J., Motornenko A., Steinhilber J., Stöcker H., 2023, *Phys. Rev. Lett.*, **131**, 191201
- Jardine R., Powell J., Müller B., 2022, *MNRAS*, **510**, 5535
- Klimenko S., et al., 2016, *Phys. Rev. D*, **93**, 042004
- Klimenko S., et al., 2021, cWB pipeline library: 6.4.0, doi:10.5281/zenodo.4419902, <https://doi.org/10.5281/zenodo.4419902>
- Kotake K., Iwakami W., Ohnishi N., Yamada S., 2009, *ApJ*, **697**, L133
- Kotake K., Iwakami-Nakano W., Ohnishi N., 2011, *ApJ*, **736**, 124
- Kuroda T., Takiwaki T., Kotake K., 2014, *Phys. Rev. D*, **89**, 044011
- Kuroda T., Kotake K., Takiwaki T., 2016, *ApJ*, **829**, L14
- Kuroda T., Kotake K., Hayama K., Takiwaki T., 2017, *ApJ*, **851**, 62
- LIGO Scientific Collaboration 2022, Technical Report T2000012-v2, Noise curves used for Simulations in the update of the Observing Scenarios Paper, <https://dcc.ligo.org/LIGO-T2000012/public>, LIGO, <https://dcc.ligo.org/LIGO-T2000012/public>
- López M., Di Palma I., Drago M., Cerdá-Durán P., Ricci F., 2021, *Phys. Rev. D*, **103**, 063011
- Macleod D. M., Areeda J. S., Coughlin S. B., Massinger T. J., Urban A. L., 2021, *SoftwareX*, **13**, 100657
- Magee R., Sharma R., Agrawal A., Udall R., 2024, *arXiv e-prints*, p. [arXiv:2410.15513](https://arxiv.org/abs/2410.15513)
- Maggiore M., 2007, Gravitational Waves: Volume 1: Theory and Experiments. Oxford University Press, doi:10.1093/acprof:oso/9780198570745.001.0001, <https://doi.org/10.1093/acprof:oso/9780198570745.001.0001>
- Marek A., Janka H. T., Müller E., 2009, *A&A*, **496**, 475
- Mezzacappa A., et al., 2020, *Phys. Rev. D*, **102**, 023027
- Mezzacappa A., et al., 2023, *Phys. Rev. D*, **107**, 043008
- Mitra A., Shukirgaliyev B., Abylkairov Y. S., Abdikamalov E., 2023, *MNRAS*, **520**, 2473
- Morozova V., Radice D., Burrows A., Vartanyan D., 2018, *ApJ*, **861**, 10
- Mueller E., Janka H. T., 1997, *A&A*, **317**, 140
- Mukherjee S., Nurbek G., Valdez O., 2021, *Phys. Rev. D*, **103**, 103008
- Müller E., Janka H. T., Wongwathanarat A., 2012, *A&A*, **537**, A63
- Müller B., Janka H.-T., Marek A., 2013, *ApJ*, **766**, 43
- Murphy J. W., Ott C. D., Burrows A., 2009, *ApJ*, **707**, 1173
- Nitz A. H., Dent T., Dal Canton T., Fairhurst S., Brown D. A., 2017, *Astrophys. J.*, **849**, 118
- Nitz A., et al., 2024, gwastro/pycbc: v2.3.3 release of PyCBC, doi:10.5281/zenodo.10473621, <https://doi.org/10.5281/zenodo.10473621>
- O'Connor E. P., Couch S. M., 2018, *ApJ*, **865**, 81
- Pajkos M. A., VanCamp S. J., Pan K.-C., Vartanyan D., Deppe N., Couch S. M., 2023, *ApJ*, **959**, 21
- Pan K.-C., Liebendörfer M., Couch S. M., Thielemann F.-K., 2021, *ApJ*, **914**, 140
- Powell J., 2018, *Classical and Quantum Gravity*, **35**, 155017
- Powell J., Müller B., 2019, *MNRAS*, **487**, 1178
- Powell J., Müller B., 2020, *MNRAS*, **494**, 4665
- Powell J., Müller B., 2022, *Phys. Rev. D*, **105**, 063018
- Powell J., Gossan S. E., Logue J., Heng I. S., 2016, *Phys. Rev. D*, **94**, 123012
- Powell J., Szczepanczyk M., Heng I. S., 2017, *Phys. Rev. D*, **96**, 123013
- Powell J., Müller B., Aguilera-Dena D. R., Langer N., 2023, *MNRAS*, **522**, 6070
- Radice D., Morozova V., Burrows A., Vartanyan D., Nagakura H., 2019, *ApJ*, **876**, L9
- Raynaud R., Cerdá-Durán P., Guilet J., 2022, *MNRAS*, **509**, 3410
- Raza N., McIver J., Dálya G., Raffai P., 2022, *Phys. Rev. D*, **106**, 063014
- Richardson C. J., Zanolin M., Andresen H., Szczepanczyk M. J., Gill K., Wongwathanarat A., 2022, *Phys. Rev. D*, **105**, 103008
- Richardson C. J., Andresen H., Mezzacappa A., Zanolin M., Benjamin M. G., Marronetti P., Lentz E. J., Szczepanczyk M. J., 2024, *arXiv e-prints*, p. [arXiv:2404.02131](https://arxiv.org/abs/2404.02131)
- Rodríguez M. C., Ranea-Sandoval I. F., Chirenti C., Radice D., 2023, *MNRAS*, **523**, 2236
- Roma V., Powell J., Heng I. S., Frey R., 2019, *Phys. Rev. D*, **99**, 063018
- Scheidegger S., Käppeli R., Whitehouse S. C., Fischer T., Liebendörfer M., 2010, *A&A*, **514**, A51
- Shibagaki S., Kuroda T., Kotake K., Takiwaki T., 2020, *MNRAS*, **493**, L138
- Smith L., Ghosh S., Sun J., Gayathri V., Heng I. S., Pai A., 2024, *Phys. Rev. D*, **110**, 083032
- Sotani H., Takiwaki T., 2016, *Phys. Rev. D*, **94**, 044043
- Sotani H., Kuroda T., Takiwaki T., Kotake K., 2019, *Phys. Rev. D*, **99**, 123024
- Sotani H., Takiwaki T., Togashi H., 2021, *Phys. Rev. D*, **104**, 123009
- Srivastava V., Ballmer S., Brown D. A., Afle C., Burrows A., Radice D., Vartanyan D., 2019, *Phys. Rev. D*, **100**, 043026
- Summerscales T. Z., Burrows A., Finn L. S., Ott C. D., 2008, *ApJ*, **678**, 1142
- Szczepanczyk M. J., et al., 2021, *Phys. Rev. D*, **104**, 102002
- Szczepanczyk M. J., et al., 2023, *Phys. Rev. D*, **107**, 062002
- Szczepanczyk M. J., et al., 2024, *Phys. Rev. D*, **110**, 042007
- Takiwaki T., Kotake K., 2018, *MNRAS*, **475**, L91
- Takiwaki T., Kotake K., Foglizzo T., 2021, *MNRAS*, **508**, 966
- Tamborra I., Hanke F., Müller B., Janka H.-T., Raffelt G., 2013, *Phys. Rev. Lett.*, **111**, 121104
- Tolley A. E., Cabourn Davies G. S., Harry I. W., Lundgren A. P., 2023, *Classical and Quantum Gravity*, **40**, 165005
- Torres-Forné A., Cerdá-Durán P., Passamonti A., Font J. A., 2018, *MNRAS*, **474**, 5272
- Torres-Forné A., Cerdá-Durán P., Obergaulinger M., Müller B., Font J. A., 2019a, *Phys. Rev. Lett.*, **123**, 051102
- Torres-Forné A., Cerdá-Durán P., Passamonti A., Obergaulinger M., Font J. A., 2019b, *MNRAS*, **482**, 3967
- Turner M. S., 1978, *Nature*, **274**, 565
- Vartanyan D., Burrows A., 2020, *ApJ*, **901**, 108
- Vartanyan D., Coleman M. S. B., Burrows A., 2022, *MNRAS*, **510**, 4689
- Vartanyan D., Burrows A., Wang T., Coleman M. S. B., White C. J., 2023, *Phys. Rev. D*, **107**, 103015
- Virtanen P., et al., 2020, *Nature Methods*, **17**, 261
- Wolfe N. E., Fröhlich C., Miller J. M., Torres-Forné A., Cerdá-Durán P., 2023, *ApJ*, **954**, 161
- Yakunin K. N., et al., 2010, *Classical and Quantum Gravity*, **27**, 194005
- Yakunin K. N., et al., 2015, *Phys. Rev. D*, **92**, 084040
- Yokozawa T., Asano M., Kayano T., Suwa Y., Kanda N., Koshio Y., Vagins M. R., 2015, *ApJ*, **811**, 86
- Zha S., O'Connor E. P., Chu M.-c., Lin L.-M., Couch S. M., 2020, *Phys. Rev. Lett.*, **125**, 051102
- Zha S., Eggenberger Andersen O., O'Connor E. P., 2024, *Phys. Rev. D*, **109**, 083023

This paper has been typeset from a $\text{\TeX}/\text{\LaTeX}$ file prepared by the author.